Modelling soot formation in a benchmark ethylene stagnation flame with a new detailed population balance model

Dingyu Hou[a,b,e], Casper S. Lindberg[c,e], Manoel Y. Manuputty[c,e], Xiaoqing You[a,b,*], Markus Kraft[c,d,e,*]

[a] *Center for Combustion Energy, Tsinghua University, Beijing, 100084, China*
[b] *Key Laboratory for Thermal Science and Power Engineering of the Ministry of Education, Tsinghua University, Beijing, 100084, China*
[c] *Department of Chemical Engineering and Biotechnology, University of Cambridge, Philippa Fawcett Drive, Cambridge, CB3 0AS, United Kingdom*
[d] *School of Chemical and Biomedical, Engineering, Nanyang Technological University, 62 Nanyang Drive, 637459, Singapore*
[e] *Cambridge Center for Advanced Research and Education in Singapore (CARES), CREATE Tower, 1 Create Way, 138602, Singapore*

Abstract

Numerical simulation of soot formation in a laminar premixed burner-stabilised benchmark ethylene stagnation flame was performed with a new detailed population balance model employing a two-step simulation methodology. In this model, soot particles are represented as aggregates composed of overlapping primary particles, where each primary particle is composed of a number of polycyclic aromatic hydrocarbons (PAHs). Coordinates of primary particles are tracked, which enables simulation on particle morphology and provides more quantities that are directly comparable to experimental observations. Parametric sensitivity study on the computed particle size distributions (PSDs) shows that the rate of production of pyrene and the collision efficiency have the most significant effect on the computed PSDs. Sensitivity of aggregate morphology to the sintering rate is studied by analysing the simulated primary particle size distributions (PPSDs) and transmission electron microscopy (TEM) images. The capability of the new model to predict PSDs in a premixed stagnation flame is investigated. Excellent agreement between the computed and measured PSDs is obtained for large burner-stagnation plate separation (≥ 0.7 cm) and for particles with mobility diameter larger than 6 nm, demonstrating the ability of this new model to describe the coagulation process of aggregate particles.

Keywords: soot model, population balance simulation, sensitivity analysis, aggregate morphology

1. Introduction

Soot is one of the by-products of the incomplete combustion of fossil fuels under global or local fuel-rich conditions. Research interest in soot mainly stems from environmental and health concerns, as well as the prospect of improving the utilization efficiency of fossil energy resources [1–3].

Extensive experimental studies have been conducted during the past several decades to explore the underlying mechanism of soot formation. These studies focused on various aspects of soot particles, including their global properties, size, morphology and chemical composition, etc. For instance, the soot volume fraction has been measured by light extinction and scattering [4] and laser light incandescence [5]; the evolution of the particle size distribution (PSD) has been obtained by scanning mobility particle sizer (SMPS) [6–12]; particle morphology has been studied using transmission electron microscopy (TEM) [12] and atomic force microscopy (AFM) [9]; the internal particle structure has been revealed in more detail through high-resolution transmission electron microscopy (HRTEM) [13–15]; the chemical composition of soot has been analyzed by laser microprobe spectroscopy [16, 17] and photoionisation aerosol mass spectroscopy [18].

However, despite all the progress made by experimental studies on the soot formation mechanism, large gaps still exist in our fundamental understanding of individual soot processes. For instance, nucleation and surface growth

*Corresponding author
Email addresses: xiaoqing.you@mail.tsinghua.edu.cn (Xiaoqing You), mk306@cam.ac.uk (Markus Kraft)

of soot still remain open questions, since it is difficult for experiments to separate these complex and competitive sooting processes and investigate them individually. Hence, to get a better understanding of soot formation, detailed modelling studies performed alongside experiments are of vital importance.

Two key aspects of soot modelling are: the physical description of soot particles and the numerical methods employed to solve the governing population balance equations (PBEs). The physical description of particles means the internal coordinates or type space used to describe a simulated particle. The evolution of particle system is described by PBEs, which are usually based on Smoluchowski's equation [19] with additional terms for soot nucleation, surface growth, condensation, oxidation and sintering, etc.

As far as the physical description is concerned, the simplest way to represent soot particles is a coalescing sphere model, which describes all particles as spheres of common density [20, 21]. A subsequent surface-volume model is slightly more detailed, describing a particle by its volume and surface area [22]. The primary particle model is the most detailed particle model discussed in the literature, which describes a nanoparticle as a sequence of primary particles [23–25]. As for the numerical methods to solve the PBEs, the three most common methods in the literature include the method of moments [26–29], discrete sectional methods [30–33] and stochastic methods [20, 25, 34–39]. The first two methods are generally restricted to one or two internal particle dimensions. By contrast, stochastic methods do not have this limitation – a member of the population of nanoparticles can have several thousand internal coordinates, which allows for a detailed description of soot particles [40]. For instance, Mitchell and Frenklach [23] investigated soot aggregation by representing a single aggregate particle as a union of intersecting spheres using a dynamic Monte-Carlo method. Morgan et al. [24] extended this simulation approach from one single aggregate to a population of aggregates. Although the model was able to capture the evolution of full structural detail of soot particles, the computational cost was so expensive that limited the further development of this detailed model.

Besides the structural information, the chemical composition of soot particles is also desirable in simulations. Since it is a general consensus in the literature that soot particles are formed from polycyclic aromatic hydrocarbons (PAHs) [1–3], the growth of PAHs attracted a great deal of research interest and various of kinetic Monte-Carlo models for PAH growth have been developed by several research groups [41–44]. Based on the primary particle model and the KMC-Aromatic Site (KMC-ARS) model [41, 42] for PAH growth, Kraft and co-workers have developed more detailed population balance models for soot by considering the detailed composition (*i.e.* PAHs) of soot particles [25, 36, 37, 41, 42, 45–47]. These models describe soot particles as aggregates composed of primary particles, which are in turn composed of individual PAHs, rather than just carbon atoms as in previous soot models. However, the aggregate morphology was not tracked in these models.

In order to simulate soot formation in flame conditions, the flame chemistry and structure need to be solved as well. The burner-stabilised stagnation (BSS) flame configuration with a nanoparticle sampling probe embedded in the stagnation plate was introduced due to its advantage of easily-defined boundary conditions for simulation [6]. The flame structure can be determined using a pseudo-one-dimensional approximation [6].

With the aforementioned detailed model and stochastic method, Yapp et al. [37] performed a population balance simulation for soot in a premixed C_2H_4 BSS flame. However, the model [37] only tracked the composition of each individual primary particle, while the relative position of these primary particles was not known. The unknown morphology of particles can result in uncertainty when comparing computed PSDs with measured ones, because mobility measurements yield the mobility diameter of particles, which is determined by aggregate morphology. If the coordinates of primary particles are not tracked, an assumption about the fractal dimension of the aggregates is required to derive their simulated mobility diameters. In addition, thermophoretic transport effects were overlooked in the post-processing step of previous study [37], yet should be accounted for as the temperature gradient is steep near the stagnation plate [48].

The **purpose of this paper** is to present a new detailed population balance model for soot, investigate its capability in predicting the PSDs in a stagnation flame and understand the influence of key model parameters on the simulated soot properties. The benchmark C_2H_4 BSS flame in Ref.[7] was chosen to be simulated with the new model, because the experimental PSDs reported in Ref.[7] were from three different laboratories and their results were in good agreement. This new model represents soot particles as aggregates composed of overlapping polydispersed primary particles, where each primary particle consists of a number of PAHs. The coordinates of all primary particles in an aggregate are tracked providing a detailed description of the particle morphology. Hence, the collision diameter (d_c) and mobility diameter (d_m) of aggregate particles can be estimated in a more reasonable way, without assuming a fractal dimension (D_f) for the aggregates, thus introducing less uncertainty when comparing with

measured PSDs. The changes in particle type space allows for a more physical model compared with our previous work [37]. A smoothing factor, which was introduced into the old model to account for particle rounding due to mass growth [25, 36], is no longer needed in the new model as the particle morphology is known. Thermophoretic transport has been accounted for in the post-process by introducing a modified simulation volume scaling term [48]. A thorough sensitivity study is carried out to understand how the model parameters effect the computed PSDs. Furthermore, the sensitivity of sintering rate to the simulated aggregate morphology is also investigated since the accurate morphology of aggregate particles is tracked.

2. Experiment

In this study, we modelled the C_2H_4 BSS flame experiment of Camacho et al. [7]. The experimental details were introduced in [6, 7]. Briefly, Camacho et al. [7] produced soot in the same benchmark ethylene-oxygen-argon premixed BSS flames (unburned gas composition (molar basis): 16.3% C_2H_4, 23.7% O_2 and 60% AR; cold gas velocity = 8.0 cm/s (STP)) at several burner-to-stagnation surface separations (H_p = 0.4, 0.45, 0.55, 0.6, 0.7, 0.8, 1.0, 1.2 cm) across three laboratories (Stanford, Shanhai Jiao Tong and Tsinghua). The temperature profiles were measured by a coated fine wire thermocouple. The same design of the sampling probe and similar mobility measurement techniques (TSI SMPS) were employed to determine the particle size distributions (PSDs).

3. Model

A detailed soot model must contain two principle components: gas-phase chemistry, which determines the flame structure, and soot particle population dynamics, which describes the evolution of the particle ensemble. Since this work aims to model soot formation in a stagnation flame, a flame model is also necessary to be coupled with the gas-phase reaction model to produce the species profiles.

3.1. Flame model

The flow in the stagnation flame is assumed to be axisymmetric and is modelled using a pseudo one-dimensional approximation, which has been described in detail by Manuputty et al. [49] and Yapp et al. [37].

3.2. Gas-phase chemistry model

The gas-phase chemistry is described by the ABF reaction mechanism [21] which contains 101 species and 543 reactions, along with a thermodynamic property file and a transport property file. The largest PAH in the ABF mechanism is pyrene (A4).

3.3. Particle model

Two different particle models – spherical model and detailed model, have been used during different simulation steps serving different purposes, which will be discussed in the methodology section (see Section 4). Since this work focuses on the detailed soot model, only a brief description on the spherical model will be given.

In the spherical model, soot particles are represented as spheres. Three types of particle processes namely inception, coagulation and surface reactions have been incorporated. Inception is modelled as the collision of two gaseous pyrene molecules, coagulation is modelled as the coalescence of two soot particles, and the surface reactions include the reactions of gaseous acetylene, hydrogen atoms, oxygen, OH and pyrene with the surface of soot particles. A more detailed description can be found in Refs. [21, 50].

In the detailed model, soot particles are represented as aggregates composed of overlapping spherical primary particles, where each primary particle consists of a number of PAHs. A4 molecules, which are the final structure in gas-phase simulation and the starting structure in particle-phase simulation, are added into the particle simulation box based on its rate of production ($\dot{\omega}_{A4}$). Growth of PAHs is described by a kinetic Monte-Carlo Aromatic Site (KMC-ARS) model [41, 42]. Two PAHs sticking together upon collisions form a primary particle. The dynamics of the soot particle population are described by the Smoluchowski equation [51] with additional terms for particle inception, surface growth, oxidation, condensation and sintering. A more detailed description of the model may be found elsewhere [25, 36, 37]. A brief description of some of the most important aspects of the model and a detailed description on new features of the current model are given below.

3.3.1. Detailed model type space

The type space is the mathematical representation of a particle. The detailed particle model type space is illustrated in Fig. 1. A particle, P_q, containing $n(P_q)$ overlapping primary particles, is represented as

$$P_q = P_q(p_1, \ldots, p_{n(P_q)}, \mathbf{D}), \tag{1}$$

where a primary particle p_i, with $i \in \{1, \ldots, n(P_q)\}$ is represented as

$$p_i = p_i(m_1, \ldots, m_{n(p_i)}, r_i, \mathbf{s_i}), \tag{2}$$

where m_x, with $x \in \{1, \ldots, n(p_i)\}$, represents the exact structure of a planar PAH and $n(p_i)$ is the total number of PAHs within the primary p_i. It is worth mentioning that the spacial arrangement of the PAHs within a primary particle is not considered in the current model, which should be one of the future work to help develop the model further. r_i is the radius of the primary particle p_i and $\mathbf{s_i}$ represents the position of the primary center relative to the center of mass of the aggregate particle. $\mathbf{D}$ is the connectivity matrix used to store the center to center separation $d_{i,j}$ of any two neighboring primaries p_i and p_j. The binary tree data structure is used to store the properties and connections of primaries within an aggregate particle as in previous work [25, 35]. More detailed discussion regarding this data structure including its merits and constraints can be found in Ref. [52]. The volume of a primary particle is calculated based on the mass of its component PAHs and the soot density ρ, represented as

$$v(p_i) = \frac{(\sum_{x=1}^{n(p_i)} \eta_{\mathrm{C}}(m_x) M_{\mathrm{C}} + \sum_{x=1}^{n(p_i)} \eta_{\mathrm{H}}(m_x) M_{\mathrm{H}})/N_{\mathrm{A}}}{\rho}, \tag{3}$$

where $\eta_y \in \mathbb{Z}, \eta_y > 0$ is the number of chemical units of type $y, y \in \{C, H\}$ [53]. M_{C} and M_{H} are the molecular weights of C and H, which are 12.01 and 1 g/mol, respectively. N_{A} is the Avogadro constant. The volume of an aggregate particle is defined as the sum of the volumes of all primary particles:

$$V(P_q) = \sum_{n=1}^{n(P_q)} v(p_i). \tag{4}$$

The diameter of a spherical primary particle without any overlaps with other primary particles is calculated as

$$d_{sph}(p_i) = \left(\frac{6v(p_i)}{\pi}\right)^{1/3}. \tag{5}$$

With the detailed particle model type space shown in Fig. 1, $v(p_i)$ can also be given by the volume of a sphere of radius r_i minus the volume of the caps created by overlaps with its neighbors as described by the equations in Ref. [52, 54]. This approach of describing aggregate particles as overlapping polydispersed primary particles is based on the work of Mitchell and Frenklach [23], Morgan et al. [24], Eggersdorfer et al. [54, 55] and Lindberg et al. [52]. The detailed model equations can be found in [52].

Particle properties that are of interest in population balance simulations, such as collision diameter (d_{c}) and mobility diameter (d_{m}), can be defined based on the aforementioned particle type space. The collision diameter is required to calculate the collision rate, while the mobility diameter needs to be determined so that it can be compared with experimental PSDs.

For a spherical particle, that is a particle containing only one primary, its mobility diameter is equal to the spherule diameter, while its collision diameter is assumed to be:

$$d_{\mathrm{c}} = \max\left(\left(\frac{6V}{\pi}\right)^{1/3}, d_{\mathrm{A}}\left(\frac{2n_{\mathrm{C}}}{3}\right)^{1/2}\right), \tag{6}$$

where the first term in the parenthesis represents the equivalent spherical diameter and the second term represents Frenklach's geometric relationship for the most condensed PAH series [37, 56]. V is the volume of the primary particle calculated from the total mass of carbon and hydrogen atoms and the density of soot material ρ. d_{A} is the size of a single aromatic ring, which is $1.395\sqrt{3}$ Å [56]. n_{C} is the maximum number of carbon atoms in a PAH within the primary particle.

For a fractal aggregate particle, characterisation of its diameter becomes more involved. Aggregates are usually characterised by their gyration diameter d_{g} or radius of gyration r_{g}. The most common definition of r_{g} and d_{g} is:

$$r_{\mathrm{g}}{}^2 = \frac{\sum_{i=1}^{n_{\mathrm{p}}} m_{\mathrm{p},i} r_i{}^2}{m}, \tag{7}$$

$$d_{\mathrm{g}} = 2r_{\mathrm{g}}, \tag{8}$$

with m and $m_{p,i}$ being the total and primary particle mass, respectively; r_i is the distance between the center of primary p_i and the center of mass of the aggregate; n_{p} is the number of primary particles within the aggregate. Primaries are treated as point masses [57]. Note that Eq. (7) will yield $r_{\mathrm{g}} = 0$ when $n_{\mathrm{p}} = 1$. Filippov et al. [58] proposed another way to calculate r_{g}, which can yield the equality of gyration and spherule radius in the limit $n_{\mathrm{p}} = 1$ as:

$$r_{\mathrm{g,F}}{}^2 = \frac{1}{n_{\mathrm{p}}} \sum_{i=1}^{n_{\mathrm{p}}} (r_i{}^2 + a_i{}^2), \tag{9}$$

where r_i is the distance between the center of primary p_i and the center of mass of the aggregate, and a_i is the sphere radius of primary p_i. Eq. (7) and Eq. (9) should yield the same r_{g} when the number of primaries within an aggregate approaches infinity. In the model, the collision diameter of aggregates follows the form of Eq. (9) as:

$$d_{\mathrm{c}} = 2r_{\mathrm{g,F}}. \tag{10}$$

The mobility diameter (d_{m}) of an aggregate can also be estimated based on its gyration diameter (d_{g}) as defined by Eq. (7) and Eq. (8) [59]:

$$d_{\mathrm{m}} = d_{\mathrm{g}} \left(\left(\frac{1}{n_{\mathrm{va}}} \right)^{0.2} + 0.4 \right), \quad n_{\mathrm{va}} > 3 \tag{11}$$

$$d_{\mathrm{m}} = d_{\mathrm{c}}, \quad n_{\mathrm{va}} \leq 3 \tag{12}$$

where n_{va} is equivalent number of primaries, calculated by:

$$n_{\mathrm{va}} = \frac{m}{m_{\mathrm{va}}} = \frac{m}{\frac{\pi}{6} d_{\mathrm{va}}{}^3 \rho}, \tag{13}$$

m_{va} is the mass of primary particle with diameter d_{va}; ρ is soot density; d_{va} is mean surface-equivalent diameter [60]:

$$d_{\mathrm{va}} = \frac{6V}{S}, \tag{14}$$

where V and S are total aggregate volume and surface area, respectively. Eq. (11) is a discrete element modelling (DEM)-derived relationship between d_{m} and d_{g} of fractal-like carbonaceous aerosols experiencing agglomeration and surface growth from free molecular to transition regime, accounting for primary particle polydispersity and aggregation [59]. Since Eq. (11) can only be applied when $n_{\mathrm{va}} > 3$, d_{m} of aggregates with $n_{\mathrm{va}} \leq 3$ is assumed to be equal to d_{c}, which is calculated by Eq. (9) and Eq. (10).

3.3.2. Detailed model particle processes

Six different particle processes – inception, coagulation, surface growth, condensation, sintering and coalescence are incorporated in the detailed model:

Inception A primary particle is formed when two PAH molecules stick after a collision. The sticking probability of these two PAHs can be determined by simple collision efficiency models in the form of a step function. If a certain criterion is satisfied for the two colliding PAHs, the sticking efficiency is 1; otherwise the sticking efficiency is 0. In the model, two parameters – inception threshold and inception mode, need to be predefined to determine the inception process. The unit of inception threshold is the number of aromatic rings. Although the starting structure in our particle population balance simulation are pyrene molecules, they can grow up to larger PAHs containing more aromatic rings based on the KMC-ARS model [42]. Assume the number of aromatic rings in two colliding PAHs are n_1 and n_2, respectively. Four different inception modes – min, max, combined or reduced represent if

$\min(n_1, n_2)$, $\max(n_1, n_2)$, $n_1 + n_2$ or $\dfrac{n_1 n_2}{n_1 + n_2}$ exceeds the inception threshold, the sticking efficiency would be 1, otherwise it would be 0 [36]. If the same inception threshold is given, inception should be the easiest with the combined mode than with other modes.

Coagulation An aggregate is formed when two particles (primary or aggregate) stick in point contact after collision. The rate of collision is determined by a collision efficiency of particles ($0 \leq A \leq 1$) and a transition regime coagulation kernel, which is dependent on the mass and collision diameter of each collision partner [61]. The orientations of colliding particles and point of contact are determined by ballistic cluster-cluster aggregation (BCCA) with a random impact parameter [62]. A more detailed description can be found in Ref. [52].

Surface growth PAHs in a primary particle can grow via surface reactions with gas-phase species, which is described by the KMC-ARS model [36, 41, 42]. In the KMC-ARS model, the rate of PAH growth processes are modelled based on reactions at radical sites together with steady-state assumption. Having noticed the fact that PAHs in large primary particle may grow slower compared with that in gas-phase as it is more difficult for gas-phase species such as H and C_2H_2 to diffuse to interior PAHs inside a large primary, two free parameters – the critical number of PAHs n_{crit} and growth factor g are introduced to differentiate PAH growth in a large primary particle and a small one. If the number of PAHs inside a primary particle exceeds n_{crit}, a growth factor $g \in [0, 1]$ will be applied to the growth rate as a multiplier of all PAHs within that primary particle [25].

In the previous model, a free parameter – smoothing factor s was introduced to account for the particle rounding due mass growth [25, 36, 37]. However, this rounding effect can be incorporated without s in the new model, because soot particles are modelled as overlapping spheres with mass added to the free surface. A particle undergoing surface growth means all PAHs inside it will be updated according to the KMC-ARS model. Taking the growth of a certain primary p_i in one aggregate as an example: total mass growth of p_i during a certain time step can be calculated by subtracting the total mass of PAHs inside p_i before surface growth from the total mass of the PAHs inside p_i after surface growth. Then this increased mass will be added to the free surface of p_i, at the same time assuming the position and radii of all other primary particles within this aggregate do not change, hence the aggregate becomes rounder. A detailed mathematical description of surface growth based on the aforementioned particle type space can be found in [52].

Condensation A particle can grow via condensation of a gas-phase PAH, following a collision between the PAH and a particle (primary or aggregate). The rate of condensation is calculated in the same manner as coagulation (transition regime collision kernel), except that one of the collision partner is a PAH molecule. The collision diameter of a PAH molecule can be estimated according to its number of carbon atoms, as shown by the second term of Eq. (6). A free model parameter – the condensation threshold, is introduced to describe the collision efficiency of the collision between the particle and the PAH molecule. If the number of aromatic rings of the colliding PAH molecule exceeds the condensation threshold (in units of the number of aromatic rings), the sticking efficiency would be 1, otherwise the sticking efficiency is 0. Condensation of PAHs on an aggregate can also make the particle more round in a similar way to surface growth.

Sintering Sintering is performed individually on each pair of neighboring primaries p_i and p_j in an aggregate, which are neighbors in an aggregate. The centers of p_i and p_j approach each other during sintering, while their masses are conserved, so the diameters of p_i and p_j also increase. Meanwhile, the positions of all other primary particles within the aggregate, except p_i and p_j, will be adjusted accordingly, due to the assumption that all other neck areas are unchanged when sintering is performed on p_i and p_j. A detailed mathematical description of sintering based on the aforementioned particle type space can be found elsewhere [52, 54]. The characteristic sintering time is given by [63]:

$$\tau_{\text{s}} = A_{\text{s}} d_{i,j} \exp\left[\frac{E_{\text{s}}}{T}\left(1 - \frac{d_{\text{crit}}}{d_{i,j}}\right)\right], \tag{15}$$

with A_{s} being the pre-exponential factor, $d_{i,j}$ being the minimum diameter of two neighboring primary particles, E_{s} being the activation energy and d_{crit} being the critical primary particle diameter below which the primaries are assumed to be liquid-like and will "coalesce" instantaneously. The sintering level s, a descriptor for the degree of sintering between two neighboring primaries, is defined as:

$$s = \frac{r_{i,j}}{R_{i,j}}, \tag{16}$$

where $r_{i,j}$ and $R_{i,j}$ are the smaller radius and neck radius of p_i and p_j, respectively. Two neighboring primary

particles will merge into one larger primary particle if $s \geq 0.95$. Besides sintering, surface growth and condensation can also cause an increase in the sintering level.

Coalescence Coalescence refers to the process by which two nascent spherical soot particles fuse into a larger spherical particle instantaneously after colliding with each other. This infinitely fast restructuring process is due to the liquid-like nature of nascent soot particles [16]. It is pertinent to mention that the sintering model in the form of Eq. (15) also accounts for coalescence of nascent soot particles. If the smaller particle between the two colliding nascent particles has a diameter less than d_{crit}, Eq. (15) will produce a infinitely small τ_{s} (comparing to the characteristic collision time), thus leading to a coalescence process.

4. Numerical method

The numerical method consists of two parts. The first simulation step couples the gas-phase chemistry, flow and a spherical particle model solved by method of moments with interpolative closure (MoMIC) [26] to calculate the flame profile. The gas-phase species concentrations, temperature and convective and thermophoretic velocities are then supplied as input into the second simulation – the post-process. These need to be expressed in terms of the residence time of a Lagrangian particle travelling from burner to stagnation plate. The conversion from distance to residence time was performed using the combined axial convective velocity and thermophoretic velocity [6]. The second simulation step post-processes the flame profile with the detailed particle model solved by stochastic method to resolve the morphology of the soot particles. A similar two-step simulation methodology has been used successfully to simulate soot formation in laminar premixed flames without a stagnation surface [36]. In this work, an improved post-processing method proposed by Lindberg et al. [48] which is capable of accounting for thermophoretic transport effects is employed to perform the population balance simulations. More detailed discussion on the two-step methodology used in this work may be found in [48].

4.1. Flame solver

The gas-phase flame structure simulation is performed using *k*inetic® software package [64], with a one-dimensional stagnation flow approximation. ABF gas-phase chemistry [21], together with a thermodynamic property file and a transport property file are supplied as input. The temperature profile is given based on experimental measurements, so the energy equation does not need to be solved. Other governing equations including the continuity equation, momentum equation, species transport equation and transport equations for the first six moments of particle size distribution (PSD) based on the spherical soot model (in Section 3.3) may be found in [37, 49]. The effect of inception and surface reaction on key gas-phase species profile can be approximately accounted for in this way. MoMIC [26] is used to close the moment transport equations [26]. These equations are solved as a boundary-value problem with boundary conditions specified according to experimental conditions, employing a damped Newton search algorithm to obtain the steady-state solutions. Manuputty et al. [49] have discussed the simulation of premixed stagnation flame in detail.

4.2. Stochastic particle population balance solver

The particle population balance is solved using a Monte Carlo method [20], with various enhancements to improve the efficiency. A majorant kernel and fictitious jump are used to speed up the calculation of coagulation rate [34, 61]. A linear process deferment algorithm (LPDA) is employed to improve the efficiency of performing surface growth and sintering [65].

To account for the significant thermophoretic transport effects caused by the strong temperature gradients near the stagnation surface in BSS flame, a correction to the post-process through a modified simulation sample volume scaling term has been introduced. This thermophoretic correction method is discussed in detail by Lindberg et al. [48].

5. Results and discussion

5.1. Thermophoretic correction

Figure 2 shows the effect of applying the thermophoretic correction [48] to the post-processing step on soot volume fraction (F_{v}) using stochastic method for the C_2H_4 BSS flame with a stagnation plate height $H_{\text{p}} = 1.2$ cm.

In order to compare the results obtained by the method of moments and those from post-processing the gas-phase profile using the stochastic method, the same particle model – spherical model, is used in both simulations. Figure 2 indicates that F_v obtained by post-processing by the thermophoretic correction (red dash line) is in agreement with the result predicted by method of moments (black solid line). However, if the post-process is performed without the thermophoretic correction, F_v is overestimated by more than a factor of two near the stagnation surface, where the temperature drops steeply, as shown by the blue dash-dot line in Fig. 2. Thus, the two-step methodology that accounts for thermophoresis is necessary to ensure that the soot particle population dynamics and integral properties are correctly simulated in the presence of a strong temperature gradient.

5.2. Parametric sensitivity analysis

All the free model parameters in this new model need to be assigned a value. Some of the most important parameters including their range, initial values and references are listed in Table 1. The meaning of these model parameters have been explained in Section 3.3. In the following sensitivity studies, all the parameters are assigned with their initial values except the parameter of which the sensitivity is investigated. Since the dominant soot particle process can be different within flames with different structure, *i.e.* flames with low stagnation plate height (H_p) and with high H_p, PSD sensitivity studies for different model parameters are performed for flames with two different H_p.

Generally speaking, for flames with relatively low H_p (*i.e.* $H_p < 0.6$ cm), the dominant soot processes are inception, coalescence and surface growth, because the soot particle residence time is too short for them to coagulate and form fractal-like aggregates. Hence, at this stage, the soot particles are nearly spherical, which has been reported by a number of experimental studies [10, 66–68]. The near-spherical morphology of nascent soot particles can be used to simplify the modeling work, because the sintering process does not need to be considered under these conditions as there are no aggregates (the sintering rate can be regarded as infinitely fast); thus leaving us fewer free model parameters to investigate. In contrast, for flames with relatively high H_p (*i.e.* $H_p > 0.6$ cm), the residence time is long enough for soot particles to coagulate and form aggregates, so coagulation becomes the dominant process rather than inception. As most soot particles are in aggregate structures when sampled at high flame height, the sintering process needs to be taken into consideration.

Based on these different features of particle processes within flames with different H_p, the sensitivity of the computed PSDs to parameters including the inception threshold, condensation threshold, inception mode, soot density, rate of production of A4 ($\dot{\omega}_{A4}$) and collision efficiency (A) are studied for a flame with $H_p = 0.45$ cm; while the sensitivity of the computed PSDs to the growth factor g and sintering model parameter d_{crit} are investigated for flame with $H_p = 1.2$ cm. The objective of the parametric sensitivity study is to understand the different influence of these key model parameters on the predicted PSDs.

5.2.1. Flame with $H_p = 0.45$ cm

As mentioned before, all soot particles are forced to be spherical during the simulation for flame with $H_p = 0.45$ cm, meaning all collisions between particles lead to coalescence rather than coagulation. Figures 3(a)–(c) show that the inception threshold, condensation threshold and inception mode have little effect on the tail of the PSDs, although they can effect the shape of the simulated PSDs significantly when particle diameters are smaller than 3 nm. It is worth mentioning that the lower limit of particle diameter is 2.5 nm from experiments, while the smallest particle diameter in simulation is only 0.87 nm, which is the size of a single pyrene molecule. Due to the lack of experimental data for sub-2.5 nm particles, it is hard to make any inference towards the soot nucleation mechanism using the simulated PSDs. Since a recent experimental work by Wang et al. [68] reported that the mass density of nascent soot particles in premixed ethylene flames can be as low as 0.6 g/cm^3, so four densities (from 0.6 to 1.8 g/cm^3) are chosen to perform the sensitivity study. Soot density has an obvious effect on the position of the PSDs as shown in Fig. 3(d). However, changes in soot density will only cause a translation of the simulated PSDs, while the shape of PSD almost stays unchanged. Figure 3 also shows that agreement between the simulated PSDs and the experimental measurements cannot be achieved by adjusting the inception threshold, condensation threshold or inception mode. Changing the soot density may result in a better agreement but cannot be correct, as the density has to be larger than 1.8 g/cm^3 to do so, which go beyond the upper limit.

Figure 4 shows the sensitivity of simulated PSDs to the rate of production of A4 ($\dot{\omega}_{A4}$) and the collision efficiency (A). The $\dot{\omega}_{A4}$ profile is calculated by solving a set of governing equations coupled to gas-phase chemistry, flow model and the first six particle moments using MoMIC, as introduced in Section 4. In a rigorous sense, $\dot{\omega}_{A4}$ is a set of

input data rather than a free parameter of the model. To study the sensitivity of the computed PSDs to $\dot{\omega}_{A4}$, two multipliers, 0.5 and 0.1 are applied to the original $\dot{\omega}_{A4}$ profile to produce the new input data for the simulation. The simulated PSDs are plotted in Fig. 4(a). Larger $\dot{\omega}_{A4}$ will shift the PSD to the right, because larger $\dot{\omega}_{A4}$ will result in more soot nuclei. In Fig. 4(b), the simulated PSDs with a collision efficiency ranging from 0.01 to 1.0 are displayed. Larger collision efficiency will produce larger soot particles at the expense of reducing the number of small particles. Both $\dot{\omega}_{A4}$ and collision efficiency A have significant effects on the simulated PSDs.

5.2.2. Flame with $H_p = 1.2$ cm

As soot aggregates are typically observed in flames with $H_p > 0.6$ cm, so the aggregate structure must be considered when performing population balance simulation for $H_p = 1.2$ cm. Figure 5 shows the sensitivity of the simulated PSDs to the growth factor g. As introduced in Section 3.3, g is a multiplier applied to the growth rate when the number of PAHs in a primary particle exceeds n_{crit}, intended to differentiate the growth rate for gas-phase PAHs and large soot particles. Since n_{crit} is hard to estimate unless the spatial arrangement of PAHs in a primary is known, we simply choose 50 as used in earlier studies [36, 37]. The simulated PSDs are not very sensitive to the growth factor g, as $g = 1.0$ (black solid line) and $g = 0.0263$ (red dash-dot line) produce very similar PSDs in Fig. 5. (0.0263 is the optimized value by Chen et al. [36].) This result seems to be a little unexpected at first, yet the lower sensitivity of g can be well explained by examining the concentration of H atom and the ratio of primary particles containing more than n_{crit} (*i.e.* 50) PAHs against the equivalent residence time, which are shown in Fig. 6. The percentage of larger primary particles (primary particles with $n_{PAH} \geq 50$) exceeds 50% after a residence time of 0.02 s. At this time, the concentration of H atoms is below 10^{-5}, which means surface growth is nearly stopped after 0.02 s based on the hydrogen-abstraction-C_2H_2-addition (HACA) surface growth mechanism [69]. Hence, it does not matter whether a factor g is applied to the growth rate or not.

The sensitivity of the computed PSDs to the sintering rate is shown in Fig. 7. The sintering rate is given by Eq. (15). To investigate the sensitivity of the computed PSDs to the sintering rate, d_{crit} is varied while other parameters in the sintering model, A_s and E_s are given the same value as estimated by Chen et al. [36] (see Table 1). d_{crit} is of interest because it is a critical parameter above which macroscopic expressions for sintering process are applied, while below which neighboring primary particles will coalescence instantaneously [63]. Figure 7 shows that the simulated PSD with $d_{crit} = 1.58$ nm (black solid line) and $d_{crit} = 5.0$ nm (red dash-dot line) are quite close to each other, except for when the particle diameters are smaller than 6 nm. The blue dash line in Fig. 7 represents an extreme case in which sintering process is excluded during the simulation. This indicates that the computed PSD is not sensitive to the sintering rate. Another extreme case in which sintering rate is infinitely fast, leading to only spherical particles is also studied, and the resulting PSD is shown as the magenta dotted line in Fig. 7. The simulated PSD simply based on spherical particle assumption can deviate a lot from experimental results, indicating that aggregate structure of soot particles does need to be considered in soot models. One interesting point that should be mentioned here is that the magenta line begins to deviate a lot from experimental data at $d_m \approx 20$ nm, which may suggest that soot particles begin to form aggregates when mobility diameter exceeds 20 nm. This finding is consistent with the earlier modelling efforts of Kazakov and Frenklach [70], who have employed a "switch-over" diameter in the range of 25 to 30 nm to simulate soot formation considering both coagulation and aggregation. It is also in agreement with a recent experimental study on the effective density of nascent soot particles in a premixed ethylene flame, that suggests an inflection point in the effective density of nascent soot occurs at $d_m \approx 20$ nm [68]. To explain the inflection point, TEM images were examined in [68], indicating soot morphology changing from spherical-like to non-spherical shapes at $d_m \approx 20$ nm. In addition, Wang et al. [68] analyzed the primary particle size distribution (PPSD) of aggregate particles with $d_m \approx 50$ nm based on the TEM images. As the flame condition in their work (16% C_2H_4,24% O_2,60% AR, cold gas velocity = 7 cm/s (STP), temperature at stagnation plate = 465 K) is very similar to the flame condition that is simulated in this work (16.3% C_2H_4,23.7% O_2,60% AR, cold gas velocity = 8 cm/s (STP), temperature at stagnation plate = 511 K), it could be interesting to give more comparison regarding the simulated and measured PPSD. Fig. S1 shows the simulated PPSD for aggregates with $d_m \approx 50$ nm when $d_{crit} = 1.58$ nm. The simulated median primary diameter is 9.4 nm which is close to the experimental measured value 10.44 nm. This agreement is encouraging, indicating the capability of the current model to simulate aggregate morphology. However, such comparison is not sufficient to optimize the sintering parameters such as d_{crit} because the simulated flame condition in this work is not exactly the same as in Ref.[68] and the aggregate morphology may be sensitive to the slight differences. Actually, another work focusing on simulating morphology of soot particles in premixed flames is in preparation, with the flame in Ref.[68] being the simulation target.

Although the computed PSDs are not sensitive to d_{crit}, the primary particle size distribution (PPSD) and the distribution of the number of primary particles per aggregate can be very sensitive to d_{crit}, as shown in Fig. 8. If sintering model is turned off, the diameter of more than 80% of primary particles is less than or around 5 nm (see Fig. 8(a)). Meanwhile, the distribution of the number of primaries in a particle can be very widespread — the number of primaries in a particle can reach 200 (see Fig. 8(d)). When the sintering model is turned on with $d_{\mathrm{crit}} = 1.58\,\mathrm{nm}$, most primaries are around 9.0 nm and the largest number of primaries per aggregate can reach ≈ 40 ; if $d_{\mathrm{crit}} = 5.0\,\mathrm{nm}$, most primaries can grow to 13.0 – 15.0 nm and the largest number of primaries per aggregate is reduced to about 10. This indicates that for aggregates, combination of different number of primaries and primary size may lead to similar mobility diameters, as shown in Fig. 7. This suggests that mobility diameter measurements are not enough, and more experimental results such as TEM images are desired for further study of sintering and coalescence of soot.

Simulated TEM-style images of soot particles with different characteristic mobility diameters ($\approx$ 10, 20, 30 and 50 nm) are displayed in Fig. 9. It is worth emphasizing that one of the biggest advantages of this new model compared to other soot models is that TEM-like images of soot particles can be generated from simulation results, because the coordinates of primary particles are tracked. An assumption about the fractal dimension of soot aggregates is no longer needed.

Since primary particles grow larger either by sintering/coalescence or surface growth, it is interesting to investigate the relative contribution to the growth of primaries of these two processes. Here we do not differentiate between sintering and coalescence since they are similar in nature — primary particles become larger through these two processes by restructuring themselves rather than by gaining mass from gas-phase species. Moreover, the sintering model used in the detailed population balance simulations does have the advantage of accounting for the coalescence of nascent soot as discussed in Section 3.3.2. Figure 10 shows the evolution of the average primary particle diameter (left axis) with time. In order to demonstrate the effect of surface growth, the concentration of H atoms (right axis) against particle residence time is also shown. The growth of primary particles nearly stops after 0.03 s, meaning that sintering/coalescence and surface growth slowed significantly after 0.03 s. In fact, after 0.02 s, the mole fraction of H atoms is almost below 10^{-5}, and the HACA surface growth can hardly take place with so few H atoms. When the sintering rate is set to zero, which in fact also excludes the coalescence of nascent soot particles, the eventual average primary particle size is around 5 nm (see the black dot line in Fig. 10), indicating that surface growth alone can only result in a primary size of about 5 nm and sintering/coalescence plays a very important role in the growth of primary particles.

Table 1 summarizes the results of the parametric sensitivity study. Among all the parameters listed in Table 1, the simulated PSD is most sensitive to the rate of production of A4 ($\dot{\omega}_{\mathrm{A4}}$) and the collision efficiency (A). It is also sensitive to the soot density (ρ), but the change in density will only cause a translation of the simulated PSD, while the shape is unchanged. The computed PSDs are not sensitive to the inception mode, inception threshold, condensation threshold, growth factor g or sintering model parameter d_{crit}, especially for larger particles. However, the morphology of the simulated soot particles can be very sensitive to d_{crit}. The knowledge gained from the parametric sensitivity study can facilitate better analysis when comparing the simulated PSDs with the measured ones under other flame conditions (flames with other H_{p}), i.e. locate which parameters may have caused the discrepancies between simulation and experiment results.

5.3. Particle size distribution

Population balance simulations at several H_{p} (0.45, 0.55, 0.6, 0.7, 0.8, 1.0, 1.2 cm) are performed using the value of free model parameters listed in Table 1, with collision efficiency $A = 1$, and rate of production of A4 ($\dot{\omega}_{\mathrm{A4}}$) determined by the method of moments with ABF gas-phase chemistry. Unlike the parametric sensitivity study in section 5.2.1, here the spherical particle assumption is not made even at low H_{p}, although the particles are still approximately spherical at low H_{p} with the detailed model.

The computed PSDs are displayed in Fig. 11. Despite the predicted PSDs being in qualitative agreement with experimental data, obvious discrepancies still exist, especially for flames with lower H_{p} (i.e. 0.45, 0.55 cm). Moreover, the prediction of small particles with mobility diameter d_{m} less than 4 nm is poor for all H_{p}. However, the poor performance of the prediction of small soot particles can be expected for a number of reasons. First, the soot nucleation mechanism is still under exploration. The nucleation process in this detailed soot model is described as any two PAHs with the sum of the number of six-member rings exceeding 32 colliding and then sticking together to form nuclei. While this is clearly an approximation, current soot modelling work has to compromise due to the

Table 1: Model parameters and their sensitivity to PSD.

Parameter	Range	Value	Ref.	Sens.[1]
(1) Material property				
Soot density, ρ (g/cm^3)	0 - 2	1.0	Totton et al. [71] Wang et al. [68]	+
(2) Nucleation				
$\dot{\omega}_{A4}$ ($mol/cm^3/s$)			Gas-phase input	++
Inception mode		Combined	this work, assigned	-
Inception threshold	> 1	32^2		-
(3) Condensation				
Condensation threshold	> 1	4^2	this work, assigned	-
(4) Surface growth				
n_{crit}	≥ 2	50	Chen et al. [36] Yapp et al. [37]	
Growth factor, g	0 - 1	1	this work, assigned	-
(5) Coagulation				
Efficiency, A	0 - 1	1	Chen et al. [36] Yapp et al. [37]	++
(6) Sintering				
A_s (s/m)	N/A	1.10×10^{-14}	Chen et al. [36] Yapp et al. [37]	
E_s (K)	1.8×10^4	9.61×10^4		
d_{crit} (nm)	1 - 5	1.58		-

[1] Sensitivity; ++ means the computed PSDs are very sensitive to this parameter; + means the computed PSDs are sensitive to this parameter; - means the computed PSDs are not sensitive to this parameter.
[2] The unit is number of six-member rings.

fact that the soot nucleation mechanism is still poorly understood. Second, PAHs start growing from A4 molecules, which are added into the particle sample volume based on their rate of production. Unfortunately, the gas-phase PAH chemistry is still far from reliable. For instance, Bakali et al. [72] reported that the A4 mole fraction in a premixed methane flame predicted by the ABF mechanism was overestimated by more than a factor of 10 compared with experiment. However, simulated PSDs can be very sensitive to the rate of production of A4 ($\dot{\omega}_{A4}$) according to the sensitivity study in section 5.2.1. Third, in the current simulation the collision efficiency is $A = 1$, which should be the upper limit. Nonetheless, many studies have pointed out that collision efficiency is size dependent [32, 73–75]. The predicted PSDs are very sensitive to the collision efficiency as discussed in section 5.2.1, it is very likely that this oversimplified collision efficiency model would cause part of the discrepancy between the simulated and experimental PSDs. Moreover, the assumption that soot density is constant $1.0\,g/cm^3$ is unlikely to be the case. According to a recent experiment study on effective density of nascent soot in a premixed C_2H_4 flame, soot density can be varying in the range from $0.6\,g/cm^3$ to $1.0\,g/cm^3$, even when soot particles are still nearly spherical [68]. This non-constant density of nascent soot may be due to the different spacial arrangement and various C/H ratio of the constituent PAHs inside a primary particle.

In contrast, the predicted PSDs at high H_p ($\geq 0.7\,cm$) are encouraging, especially for particles with mobility diameter larger than 6.0 nm. This excellent agreement is mainly because coagulation is the dominant process at higher H_p due to the drop in nucleation rate, as suggested in Ref. [23, 76] and the $\dot{\omega}_{A4}$ profile for flame with $H_p = 1.2\,cm$ in Fig. S2. Although $\dot{\omega}_{A4}$ is not the same as nucleation rate, it can reflect the variation trend of nucleation rate to some extent. Since $\dot{\omega}_{A4}$ decreased by more than one order of magnitude from its maximum value after 20 ms, nucleation became negligible after 20 ms, while the residence time for a Lagrangian particle travelling from burner to stagnation plate at 1.2 cm is more than 60 ms. In addition, after about 20 ms the surface growth rate

is very slow due to the low H atom mole fraction (below 10^{-5}, see Fig. 6). Therefore, coagulation dominates for flames with high H_{p}. It is worth emphasizing that this new model has an advantage in simulating the formation of aggregates since the coordinates of all primary particles are tracked. Most previous soot models simply assumed a constant fractal dimension of 1.8 to deal with aggregate particles [32, 36, 37, 46], while not too many modelling work paid attention to the detailed aggregate morphology in the past. Efforts on capturing more detailed morphological information of aggregates were made by Balthasar and Frenklach [76], who employed a time-varying shape factor instead of a constant fractal dimension to simulate soot formation. In our work, with the detailed geometrical information of simulated particles known, the collision diameters and mobility diameters of soot aggregates can be calculated based on their gyration diameter (see Eq. (7)) [59, 77]. Such more physical description of the coagulation process would definitely improve the model performance in predicting PSDs for larger aggregate particles.

Figure 12 shows the simulated soot particle number density (N) and volume fractions (F_{v}) compared with experimental measurements. In Fig. 12, the gray error bars show the N and F_{v} measured by experiments [7], with the upper and lower limit being the maximum and minimum measured data among four individual experimental setup [7]. The open circles are simulation results that correspond to the PSDs displayed in Fig. 11, *i*.e. simulation results by post-processing the gas-phase profile calculated by MoMIC (initial $\dot{\omega}_{\mathrm{A4}}$ and A were used). Since the lower detection limit of d_{m} in experiment is $\approx 2.5\,\mathrm{nm}$, thus to conduct a better comparison between the simulation results and the measured results, number density of particles with $d_{\mathrm{m}} \geq 2.5\,\mathrm{nm}$ are also displayed by the green symbols in Fig. 12(a) . However, this treatment cannot be applied to the MoMIC results, because the method of moments does not track the number density of particles with $d_{\mathrm{m}} < 2.5\,\mathrm{nm}$. In the method of moment, the smallest particle contains two A4 molecules, which has a $d_{\mathrm{m}} \approx 1\,\mathrm{nm}$, well below the experimental detection limit. This is part of the reasons why N predicted by MoMIC (red open triangle in Fig. 12(a)) is higher than the post-processed results (green open circle in Fig. 12(a)). When comparing the simulated volume fraction F_{v} with the measured ones, it is unnecessary to exclude particles with $d_{\mathrm{m}} < 2.5\,\mathrm{nm}$ as their contribution to the total F_{v} is rather small. Therefore, all the simulated particles are accounted for in Fig. 12(b). In general, the post-processed results do not agree well with experimental measurements, tending to underestimate both N and F_{v} at most H_{p}. At $H_{\mathrm{p}} = 0.6,\ 0.7,\ 0.8$ cm, both simulated N and F_{v} are underestimated compared with experimental results, though the error bars of experimental data are quite large. One possible explanation for the underestimation of N is that the collision efficiency $A = 1$ is overestimated.

It is worth emphasizing that the population balance simulation with the detailed soot model is a post-processing procedure based on the input gas-phase profile. This can be demonstrated by Fig. 12 in which the post-processed F_{v} and N are close to the results predicted by MoMIC. However, large uncertainties can exist in the calculated $\dot{\omega}_{\mathrm{A4}}$ profile in the first step simulation due to the fact that gas-phase PAH chemistry is far from reliable, as mentioned earlier. In Fig. 12(b), F_{v} can be either overestimated or underestimated by MoMIC for different H_{p}, suggesting the uncertainties in the input gas-phase profile for post-processing. Unfortunately, the simulated PSDs are found to be very sensitive to the input $\dot{\omega}_{\mathrm{A4}}$ profile, as discussed in the parametric sensitivity study in Section 5.2. Moreover, other parameters can hardly effect the shape of the computed PSDs except the input $\dot{\omega}_{\mathrm{A4}}$ profile and the collision efficiency A. Having realized the uncertainties in the input $\dot{\omega}_{\mathrm{A4}}$ profile and the likely to be overestimated collision efficiency A and their significant effect on the computed PSDs compared with other parameters in the detailed soot model, new population balance simulations are performed by varying input $\dot{\omega}_{\mathrm{A4}}$ profile and A, and the results are shown in Fig. 13. Better agreement between the simulated PSDs and experimental measurements is achieved, especially for flames with lower H_{p}. In addition, the post-processed integral properties of soot – the particle number density N and volume fraction F_{v} for all H_{p} are consistent with the experiments after these modifications (see the open square symbols in Fig. 12). In Fig. 13, different input $\dot{\omega}_{\mathrm{A4}}$ profile and collision efficiency A (≤ 1) are used at each individual H_{p} in order to make the simulated PSDs as close to the measured PSDs as possible. It is worth mentioning that the collision efficiency A increases with H_{p}. Since the mean particle size increases with H_{p}, Fig. 13 suggests that the collision efficiency increases with particle size, which is consistent with other studies [32, 73–75]. For instance, an experiment conducted by Sirignano and D'Anna [74] suggests that sub-10 nm nano-particles can have a sticking efficiency more than one order of magnitude lower than unity. In a more recent study, Sirignano and D'Anna [75] attributed the size-dependent sticking efficiency to the drastic drop of van der Waals interactions between small nanoparticles, which can become lower than the kinetic energy of particles at flame temperature. At $H_{\mathrm{p}} = 0.45$ and 0.55 cm in Fig. 13, a very low collision efficiency $A = 0.2$ is used to fit to the experimental PSDs, which indicates small nascent soot particles ($d_{\mathrm{m}} \leq 8$ nm) can have collision efficiencies much lower than 1. In contrast, at $H_{\mathrm{p}} = 1.2\,\mathrm{cm}$, a relatively high efficiency $A = 0.8$ is used for the purpose of fitting, indicating that

collision efficiency of large particles ($d_m \geq 20\,nm$) can be very close to 1. It should be noted that here one collision efficiency is used for one H_p, which makes the collision efficiency an average property of all particles at that H_p, since at any H_p, both small particles and large particles exist. At $H_p = 0.45$ cm, average collision efficiency $A = 0.2$ was used for all particles, yet small particles can have an efficiency much lower than 0.2 while large particles can have an efficiency higher than 0.2. Likewise, at $H_p = 1.2$ cm, the average collision efficiency $A = 0.8$ was used for all particles; however, such an efficiency must be overestimated for small particles, which leads to the number density of particles less than 5 nm being underestimated.

6. Conclusion

In this paper we have presented a new detailed population balance model for soot, which is able to track aggregate morphology as well as detailed composition of soot particles during simulation. A two-step methodology that accounts for thermophoretic transport in the post-process was employed to simulate soot formation in a benchmark laminar premixed BSS ethylene flame. A thorough parametric sensitivity study was performed to understand the influence of key model parameters on the predicted PSDs and soot particle morphology. By comparing the computed PSDs with experimental measurements and investigating the simulated soot particle morphology, we provided insight into soot formation processes and suggested future work on soot modelling.

Comparison of the soot volume fraction obtained by post-processing with and without thermophoretic correction against the MoMIC solution from the first simulation demonstrates that the thermophoretic effect must be accounted for when the temperature gradient is significant.

The parametric sensitivity study for the benchmark C_2H_4 BSS flame shows that soot PSDs are most sensitive to the rate of production of pyrene and collision efficiency based on the current model. Changes in soot density will lead to an overall shift of the simulated PSDs. Other model parameters including the inception mode, inception threshold, condensation threshold, growth factor g have little effect on the computed PSDs. The sensitivity of the simulated PSDs to the sintering rate has been studied by varying d_{crit} in the sintering model. Although the sintering rate does not have pronounced effect on the computed PSDs, the aggregate structure of soot particles does need to be considered in soot models. The predicted PSD can deviate significantly from experiments when sintering rate is infinitely fast leading to only spherical particles. Unlike the insensitivity of d_{crit} to the computed PSDs, particle morphology was found to be very sensitive to d_{crit}, which can be demonstrated by both PPSDs and simulated TEM-like images. Experimental TEMs are required to carry out further study on the sintering model of soot.

When comparing computed PSDs with the observed ones, a relatively good agreement was obtained at higher H_p ($\geq 0.7\,cm$) for particles with d_m larger than 6 nm, showing the advantage of current population balance model in describing the coagulation process of aggregate particles. However, at lower H_p ($< 0.7\,cm$) or for particles with d_m smaller than 6 nm at all H_p, simulated PSDs can deviate significantly from the measured ones. This disagreement may be attributed to the unknown nucleation mechanism for soot, relatively poor knowledge towards the gas-phase PAH chemistry, overestimated collision efficiency and nonconstant density of nascent soot. Encouraging agreement between computed and measured PSDs at all H_p was achieved after making some changes in input rate of production of A4 and collision efficiency of particles. In addition, the collision efficiency of particles was suggested to be size dependent – larger particles have a higher collision efficiency that may be close to 1 while small particles may have collision efficiency an order of magnitude lower than 1.

Nevertheless, the fact that the computed PSDs are not fully consistent with the measured ones together with the results obtained from the parametric sensitivity study suggests future work on soot modelling should focus on the following two aspects. First of all, a better understanding of soot nucleation process, especially gas-phase PAH precursor chemistry, is imperative to make further progress. Second, a more fundamental study on the collision efficiency of nascent soot particles is desired. A more detailed relationship between collision efficiency, particle size, temperature and pressure, may help to improve the agreement between computed and measured PSDs. Moreover, the detailed description of each particle in this new model yields more simulation quantities that are directly comparable to experimental observations, such as TEM images. The capability to accurately track aggregate morphology can facilitate further studies on soot processes relating to morphology evolution, such as sintering and coalescence.

Acknowledgements

This project is supported by the National Research Foundation (NRF), Prime Minister's Office, Singapore under its Campus for Research Excellence and Technological Enterprise (CREATE) programme, the National Science Foundation of China (91541122) and the Foundation of State Key Laboratory of Coal Combustion (FSKLCCA1701). The China Scholarship Council (CSC) is gratefully acknowledged. MK also acknowledges the support of the Alexander von Humboldt Foundation. CSL acknowledges the support of Venator.

References

[1] M. Frenklach, Reaction mechanism of soot formation in flames, Physical Chemistry Chemical Physics 4 (2002) 2028–2037. doi:10.1039/B110045A.

[2] H. Richter, J. Howard, Formation of polycyclic aromatic hydrocarbons and their growth to soot – a review of chemical reaction pathways, Progress in Energy and Combustion Science 26 (2000) 565 – 608. doi:10.1016/S0360-1285(00)00009-5.

[3] H. Wang, Formation of nascent soot and other condensed-phase materials in flames, Proceedings of the Combustion Institute 33 (2011) 41 – 67. doi:10.1016/j.proci.2010.09.009.

[4] M. Choi, G. Mulholland, A. Hamins, T. Kashiwagi, Comparisons of the soot volume fraction using gravimetric and light extinction techniques, Combustion and Flame 102 (1995) 161 – 169. doi:10.1016/0010-2180(94)00282-W.

[5] C. R. Shaddix, K. C. Smyth, Laser-induced incandescence measurements of soot production in steady and flickering methane, propane, and ethylene diffusion flames, Combustion and Flame 107 (1996) 418 – 452. doi:10.1016/S0010-2180(96)00107-1.

[6] A. D. Abid, J. Camacho, D. A. Sheen, H. Wang, Quantitative measurement of soot particle size distribution in premixed flames — the burner-stabilized stagnation flame approach, Combustion and Flame 156 (2009) 1862 – 1870. doi:10.1016/j.combustflame.2009.05.010.

[7] J. Camacho, C. Liu, C. Gu, H. Lin, Z. Huang, Q. Tang, X. You, C. Saggese, Y. Li, H. Jung, L. Deng, I. Wlokas, H. Wang, Mobility size and mass of nascent soot particles in a benchmark premixed ethylene flame, Combustion and Flame 162 (2015) 3810 – 3822. doi:10.1016/j.combustflame.2015.07.018.

[8] Q. Tang, R. Cai, X. You, J. Jiang, Nascent soot particle size distributions down to 1nm from a laminar premixed burner-stabilized stagnation ethylene flame, Proceedings of the Combustion Institute 36 (2017) 993 – 1000. doi:10.1016/j.proci.2016.08.085.

[9] A. Abid, E. Tolmachoff, D. Phares, H. Wang, Y. Liu, A. Laskin, Size distribution and morphology of nascent soot in premixed ethylene flames with and without benzene doping, Proceedings of the Combustion Institute 32 (2009) 681 – 688. doi:10.1016/j.proci.2008.07.023.

[10] A. D. Abid, N. Heinz, E. D. Tolmachoff, D. J. Phares, C. S. Campbell, H. Wang, On evolution of particle size distribution functions of incipient soot in premixed ethylene-oxygen-argon flames, Combustion and Flame 154 (2008) 775 – 788. doi:10.1016/j.combustflame.2008.06.009.

[11] Q. Tang, J. Mei, X. You, Effects of CO_2 addition on the evolution of particle size distribution functions in premixed ethylene flame, Combustion and Flame 165 (2016) 424 – 432. doi:10.1016/j.combustflame.2015.12.026.

[12] B. Zhao, K. Uchikawa, H. Wang, A comparative study of nanoparticles in premixed flames by scanning mobility particle sizer, small angle neutron scattering, and transmission electron microscopy, Proceedings of the Combustion Institute 31 (2007) 851 – 860. doi:10.1016/j.proci.2006.08.064.

[13] P. D. Teini, D. M. Karwat, A. Atreya, Observations of nascent soot: Molecular deposition and particle morphology, Combustion and Flame 158 (2011) 2045 – 2055. doi:10.1016/j.combustflame.2011.03.005.

[14] M. L. Botero, D. Chen, S. González-Calera, D. Jefferson, M. Kraft, HRTEM evaluation of soot particles produced by the non-premixed combustion of liquid fuels, Carbon 96 (2016) 459 – 473. doi:10.1016/j.carbon.2015.09.077.

[15] M. L. Botero, N. Eaves, J. A. Dreyer, Y. Sheng, J. Akroyd, W. Yang, M. Kraft, Experimental and numerical study of the evolution of soot primary particles in a diffusion flame, Proceedings of the Combustion Institute (2018). doi:10.1016/j.proci.2018.06.185.

[16] R. Dobbins, R. Fletcher, W. Lu, Laser microprobe analysis of soot precursor particles and carbonaceous soot, Combustion and Flame 100 (1995) 301 – 309. doi:10.1016/0010-2180(94)00047-V.

[17] R. Dobbins, R. Fletcher, H.-C. Chang, The evolution of soot precursor particles in a diffusion flame, Combustion and Flame 115 (1998) 285 – 298. doi:10.1016/S0010-2180(98)00010-8.

[18] B. Öktem, M. P. Tolocka, B. Zhao, H. Wang, M. V. Johnston, Chemical species associated with the early stage of soot growth in a laminar premixed ethylene-oxygen-argon flame, Combustion and Flame 142 (2005) 364 – 373. doi:10.1016/j.combustflame.2005.03.016.

[19] J. H. Seinfeld, S. N. Pandis, Atmospheric chemistry and physics: from air pollution to climate change, John Wiley & Sons, 2012.

[20] M. Balthasar, M. Kraft, A stochastic approach to calculate the particle size distribution function of soot particles in laminar premixed flames, Combustion and Flame 133 (2003) 289 – 298. doi:10.1016/S0010-2180(03)00003-8.

[21] J. Appel, H. Bockhorn, M. Frenklach, Kinetic modeling of soot formation with detailed chemistry and physics: laminar premixed flames of C2 hydrocarbons, Combustion and Flame 121 (2000) 122 – 136. doi:10.1016/S0010-2180(99)00135-2.

[22] R. I. Patterson, M. Kraft, Models for the aggregate structure of soot particles, Combustion and Flame 151 (2007) 160 – 172. doi:10.1016/j.combustflame.2007.04.012.

[23] P. Mitchell, M. Frenklach, Monte carlo simulation of soot aggregation with simultaneous surface growth-why primary particles appear spherical, Symposium (International) on Combustion 27 (1998) 1507 – 1514. doi:10.1016/S0082-0784(98)80558-4.

[24] N. Morgan, M. Kraft, M. Balthasar, D. Wong, M. Frenklach, P. Mitchell, Numerical simulations of soot aggregation in premixed laminar flames, Proceedings of the Combustion Institute 31 (2007) 693 – 700. doi:10.1016/j.proci.2006.08.021.

[25] M. Sander, R. I. Patterson, A. Braumann, A. Raj, M. Kraft, Developing the PAH-PP soot particle model using process informatics and uncertainty propagation, Proceedings of the Combustion Institute 33 (2011) 675 – 683. doi:10.1016/j.proci.2010.06.156.

[26] M. Frenklach, Method of moments with interpolative closure, Chemical Engineering Science 57 (2002) 2229 – 2239. doi:10.1016/S0009-2509(02)00113-6.

[27] M. Frenklach, S. J. Harris, Aerosol dynamics modeling using the method of moments, Journal of Colloid and Interface Science 118 (1987) 252 – 261. doi:10.1016/0021-9797(87)90454-1.

[28] M. Frenklach, Dynamics of discrete distribution for Smoluchowski coagulation model, Journal of Colloid and Interface Science 108 (1985) 237 – 242. doi:10.1016/0021-9797(85)90256-5.

[29] S. Wu, E. K. Y. Yapp, J. Akroyd, S. Mosbach, R. Xu, W. Yang, M. Kraft, Extension of moment projection method to the fragmentation process, Journal of Computational Physics 335 (2017) 516 – 534. doi:10.1016/j.jcp.2017.01.045.

[30] F. Gelbard, J. H. Seinfeld, Simulation of multicomponent aerosol dynamics, Journal of Colloid and Interface Science 78 (1980) 485 – 501. doi:10.1016/0021-9797(80)90587-1.

[31] S. Kumar, D. Ramkrishna, On the solution of population balance equations by discretization — i. a fixed pivot technique, Chemical Engineering Science 51 (1996) 1311 – 1332. doi:10.1016/0009-2509(96)88489-2.

[32] R. Lindstedt, B. Waldheim, Modeling of soot particle size distributions in premixed stagnation flow flames, Proceedings of the Combustion Institute 34 (2013) 1861 – 1868. doi:10.1016/j.proci.2012.05.047.

[33] C. Saggese, S. Ferrario, J. Camacho, A. Cuoci, A. Frassoldati, E. Ranzi, H. Wang, T. Faravelli, Kinetic modeling of particle size distribution of soot in a premixed burner-stabilized stagnation ethylene flame, Combustion and Flame 162 (2015) 3356 – 3369. doi:10.1016/j.combustflame.2015.06.002.

[34] M. Goodson, M. Kraft, An efficient stochastic algorithm for simulating nano-particle dynamics, Journal of Computational Physics 183 (2002) 210 – 232. doi:10.1006/jcph.2002.7192.

[35] S. Shekar, W. J. Menz, A. J. Smith, M. Kraft, W. Wagner, On a multivariate population balance model to describe the structure and composition of silica nanoparticles, Computers and Chemical Engineering 43 (2012) 130 – 147. doi:10.1016/j.compchemeng.2012.04.010.

[36] D. Chen, Z. Zainuddin, E. K. Y. Yapp, J. Akroyd, S. Mosbach, M. Kraft, A fully coupled simulation of PAH and soot growth with a population balance model, Proceedings of the Combustion Institute 34 (2013) 1827 – 1835. doi:10.1016/j.proci.2012.06.089.

[37] E. K. Y. Yapp, D. Chen, J. Akroyd, S. Mosbach, M. Kraft, J. Camacho, H. Wang, Numerical simulation and parametric sensitivity study of particle size distributions in a burner-stabilised stagnation flame, Combustion and Flame 162 (2015) 2569 – 2581. doi:10.1016/j.combustflame.2015.03.006.

[38] A. Boje, J. Akroyd, S. Sutcliffe, J. Edwards, M. Kraft, Detailed population balance modelling of TiO_2 synthesis in an industrial reactor, Chemical Engineering Science 164 (2017) 219 – 231. doi:10.1016/j.ces.2017.02.019.

[39] C. Lindberg, J. Akroyd, M. Kraft, Developing breakage models relating morphological data to the milling behaviour of flame synthesised titania particles, Chemical Engineering Science 166 (2017) 53 – 65. doi:10.1016/j.ces.2017.03.016.

[40] M. Kraft, Modelling of particulate processes, KONA Powder and Particle Journal 23 (2005) 18–35. doi:10.14356/kona.2005007.

[41] M. Celnik, A. Raj, R. West, R. Patterson, M. Kraft, Aromatic site description of soot particles, Combustion and Flame 155 (2008) 161 – 180. doi:10.1016/j.combustflame.2008.04.011.

[42] A. Raj, M. Celnik, R. Shirley, M. Sander, R. Patterson, R. West, M. Kraft, A statistical approach to develop a detailed soot growth model using PAH characteristics, Combustion and Flame 156 (2009) 896 – 913. doi:10.1016/j.combustflame.2009.01.005.

[43] A. Violi, S. Izvekov, Soot primary particle formation from multiscale coarse-grained molecular dynamics simulation, Proceedings of the Combustion Institute 31 (2007) 529 – 537. doi:10.1016/j.proci.2006.07.240.

[44] R. Whitesides, M. Frenklach, Detailed kinetic monte carlo simulations of graphene-edge growth, The Journal of Physical Chemistry A 114 (2010) 689–703. doi:10.1021/jp906541a.

[45] M. S. Celnik, M. Sander, A. Raj, R. H. West, M. Kraft, Modelling soot formation in a premixed flame using an aromatic-site soot model and an improved oxidation rate, Proceedings of the Combustion Institute 32 (2009) 639 – 646. doi:10.1016/j.proci.2008.06.062.

[46] E. K. Y. Yapp, R. I. Patterson, J. Akroyd, S. Mosbach, E. M. Adkins, J. H. Miller, M. Kraft, Numerical simulation and parametric sensitivity study of optical band gap in a laminar co-flow ethylene diffusion flame, Combustion and Flame 167 (2016) 320 – 334. doi:10.1016/j.combustflame.2016.01.033.

[47] E. K. Y. Yapp, C. G. Wells, J. Akroyd, S. Mosbach, R. Xu, M. Kraft, Modelling PAH curvature in laminar premixed flames using a detailed population balance model, Combustion and Flame 176 (2017) 172 – 180. doi:10.1016/j.combustflame.2016.10.004.

[48] C. S. Lindberg, M. Y. Manuputty, J. Akroyd, M. Kraft, A two-step simulation methodology for modelling stagnation flame synthesised aggregate nanoparticles, Combustion and Flame 202 (2019) 143 – 153. doi:10.1016/j.combustflame.2019.01.010.

[49] M. Y. Manuputty, J. Akroyd, S. Mosbach, M. Kraft, Modelling TiO_2 formation in a stagnation flame using method of moments with interpolative closure, Combustion and Flame 178 (2017) 135 – 147. doi:10.1016/j.combustflame.2017.01.005.

[50] J. Singh, Detailed soot modelling in laminar premixed flames, Ph.D. thesis, University of Cambridge, 2006.

[51] S. K. Friedlander, Smoke, dust and haze: Fundamentals of aerosol behavior, 1977.

[52] C. Lindberg, M. Y. Manuputty, E. K. Y. Yapp, J. Akroyd, M. Kraft, A detailed particle model for polydisperse titanium dioxide aggregates (2018). Manuscript submitted for publication.

[53] E. K. Y. Yapp, Numerical simulation of soot in laminar flames, Ph.D. thesis, University of Cambridge, 2016.

[54] M. L. Eggersdorfer, D. Kadau, H. J. Herrmann, S. E. Pratsinis, Multiparticle sintering dynamics: From fractal-like aggregates to compact structures, Langmuir 27 (2011) 6358–6367. doi:10.1021/la200546g.

[55] M. L. Eggersdorfer, D. Kadau, H. J. Herrmann, S. E. Pratsinis, Aggregate morphology evolution by sintering: Number and diameter of primary particles, Journal of Aerosol Science 46 (2012) 7 – 19. doi:10.1016/j.jaerosci.2011.11.005.

[56] M. Frenklach, H. Wang, Detailed mechanism and modeling of soot particle formation, in: Soot formation in combustion, Springer, 1994, pp. 165–192.

[57] M. L. Eggersdorfer, S. E. Pratsinis, Agglomerates and aggregates of nanoparticles made in the gas phase, Advanced Powder Technology 25 (2014) 71 – 90. doi:10.1016/j.apt.2013.10.010.

[58] A. Filippov, M. Zurita, D. Rosner, Fractal-like aggregates: Relation between morphology and physical properties, Journal of Colloid and Interface Science 229 (2000) 261 – 273. doi:10.1006/jcis.2000.7027.

[59] G. A. Kelesidis, E. Goudeli, S. E. Pratsinis, Morphology and mobility diameter of carbonaceous aerosols during agglomeration and surface growth, Carbon 121 (2017) 527 – 535. doi:10.1016/j.carbon.2017.06.004.

[60] M. L. Eggersdorfer, S. E. Pratsinis, The structure of agglomerates consisting of polydisperse particles, Aerosol Science and Technology 46 (2012) 347–353. doi:10.1080/02786826.2011.631956.

[61] R. I. Patterson, J. Singh, M. Balthasar, M. Kraft, W. Wagner, Extending stochastic soot simulation to higher pressures, Combustion and Flame 145 (2006) 638–642. doi:10.1016/j.combustflame.2006.02.005.

[62] R. Jullien, Transparency effects in cluster-cluster aggregation with linear trajectories, Journal of Physics A: Mathematical and General 17 (1984) L771.

[63] S. Tsantilis, H. Briesen, S. E. Pratsinis, Sintering time for silica particle growth, Aerosol Science and Technology 34 (2001) 237–246. doi:10.1080/02786820119149.

[64] CMCL Innovations, *k*inetics®, 2016.

[65] R. Patterson, J. Singh, M. Balthasar, M. Kraft, J. Norris, The linear process deferment algorithm: A new technique for solving population balance equations, SIAM Journal on Scientific Computing 28 (2006) 303–320. doi:10.1137/040618953.

[66] M. M. Maricq, An examination of soot composition in premixed hydrocarbon flames via laser ablation particle mass spectrometry, Journal of Aerosol Science 40 (2009) 844 – 857. doi:10.1016/j.jaerosci.2009.07.001.

[67] S. Marina, L. Sydnie, V. Henning, B. André, G. Armin, W. Hai, K.-H. Katharina, Imaging nanocarbon materials: Soot particles in flames are not structurally homogeneous, ChemPhysChem 14 (2013) 3248–3254. doi:10.1002/cphc.201300581.

[68] M. Wang, Q. Tang, J. Mei, X. You, On the effective density of soot particles in premixed ethylene flames, Combustion and Flame 198 (2018) 428 – 435. doi:10.1016/j.combustflame.2018.10.004.

[69] M. Frenklach, H. Wang, Detailed modeling of soot particle nucleation and growth, Symposium (International) on Combustion 23 (1991) 1559 – 1566. doi:10.1016/S0082-0784(06)80426-1.

[70] A. Kazakov, M. Frenklach, Dynamic modeling of soot particle coagulation and aggregation: Implementation with the method of moments and application to high-pressure laminar premixed flames, Combustion and Flame 114 (1998) 484 – 501. doi:10.1016/S0010-2180(97)00322-2.

[71] T. S. Totton, D. Chakrabarti, A. J. Misquitta, M. Sander, D. J. Wales, M. Kraft, Modelling the internal structure of nascent soot particles, Combustion and Flame 157 (2010) 909 – 914. doi:10.1016/j.combustflame.2009.11.013.

[72] A. E. Bakali, X. Mercier, M. Wartel, F. Acevedo, I. Burns, L. Gasnot, J.-F. Pauwels, P. Desgroux, Modeling of PAHs in low pressure sooting premixed methane flame, Energy 43 (2012) 73 – 84. doi:10.1016/j.energy.2011.12.026.

[73] A. D'Alessio, A. Barone, R. Cau, A. D'Anna, P. Minutolo, Surface deposition and coagulation efficiency of combustion generated nanoparticles in the size range from 1 to 10nm, Proceedings of the Combustion Institute 30 (2005) 2595 – 2603. doi:10.1016/j.proci.2004.08.267.

[74] M. Sirignano, A. D'Anna, Coagulation of combustion generated nanoparticles in low and intermediate temperature regimes: An experimental study, Proceedings of the Combustion Institute 34 (2013) 1877 – 1884. doi:10.1016/j.proci.2012.06.119.

[75] M. Sirignano, A. D'Anna, Filtration and coagulation efficiency of sub–10 nm combustion-generated particles, Fuel 221 (2018) 298 – 302. doi:10.1016/j.fuel.2018.02.107.

[76] M. Balthasar, M. Frenklach, Detailed kinetic modeling of soot aggregate formation in laminar premixed flames, Combustion and Flame 140 (2005) 130 – 145. doi:10.1016/j.combustflame.2004.11.004.

[77] C. M. Sorensen, The mobility of fractal aggregates: A review, Aerosol Science and Technology 45 (2011) 765–779. doi:10.1080/02786826.2011.560909.

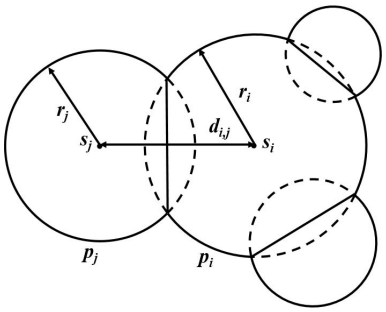

Figure 1: An illustration of the detailed particle model type space showing an aggregate particle (solid outlines) composed of primary particles modelled as overlapping spheres (indicated by the dashed lines). Redrawn based on Ref. [52]

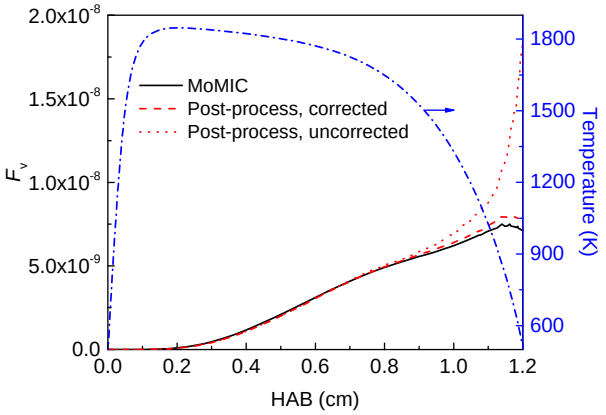

Figure 2: Effect of the thermophoretic correction on soot volume fraction (F_{v}) (left Y-axis) against height above burner (HAB). Measured temperature profile in Ref. [7] (right Y-axis) is also shown. The stagnation plate height (H_{p}) is 1.2 cm.

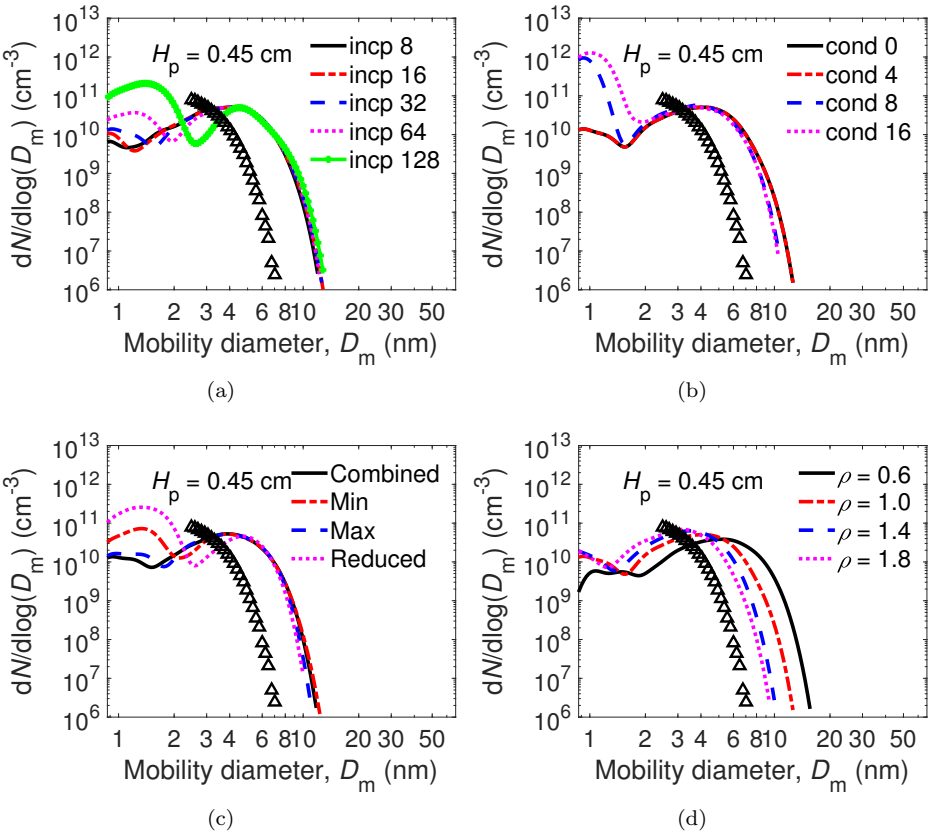

Figure 3: Sensitivity of the simulated (lines) PSDs to (a) Inception threshold; (b) Condensation threshold; (c) Inception mode; and (d) Soot density ρ; for $H_p = 0.45$ cm. Symbols are experimental data reported by Tsinghua in Ref. [7]

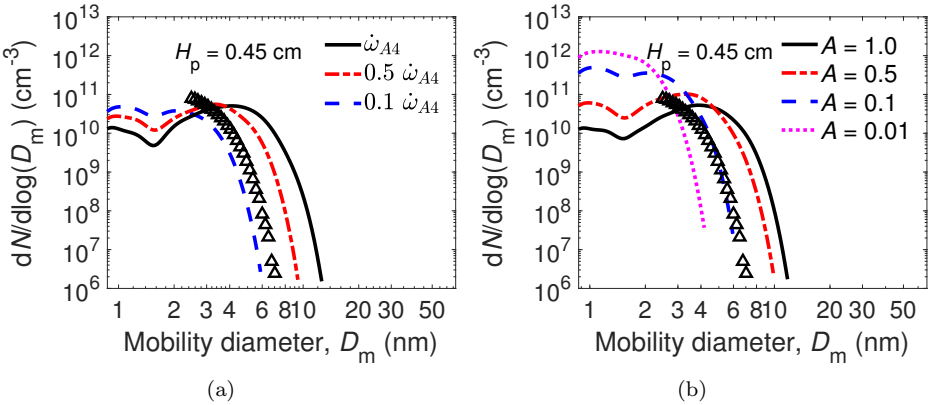

Figure 4: Sensitivity of the simulated (lines) PSDs to: (a) Rate of production of A4 ($\dot{\omega}_{A4}$); (b) Collision efficiency (A); for $H_p = 0.45$ cm. Symbols are experimental data reported by Tsinghua in Ref. [7].

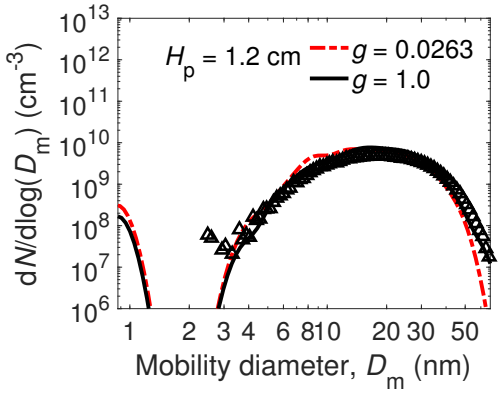

Figure 5: Sensitivity of the simulated PSDs (lines) to the growth factor g for $H_p = 1.2$ cm. Symbols are experimental data reported by Tsinghua in Ref. [7].

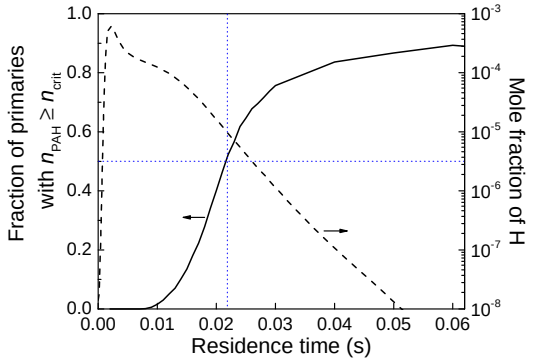

Figure 6: Fraction of primary particles with $n_{\mathrm{PAH}} > n_{\mathrm{crit}}$ (left Y-axis) and mole fraction of H atoms (right Y-axis) against residence time for $H_p = 1.2$ cm. The horizontal dotted-line shows 50% and the vertical dotted-line shows the corresponding residence time.

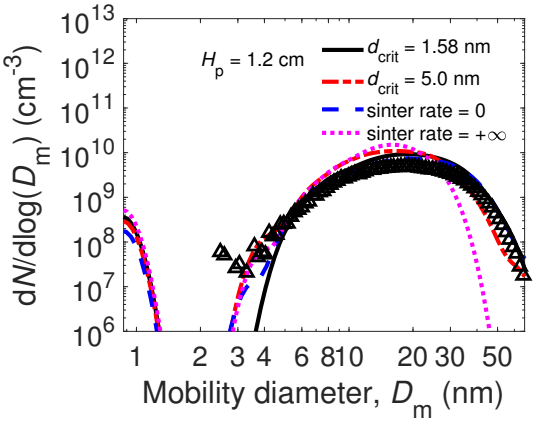

Figure 7: Sensitivity of the simulated PSDs (lines) to sintering rate for $H_p = 1.2$ cm. Symbols are experimental data reported by Tsinghua in Ref. [7].

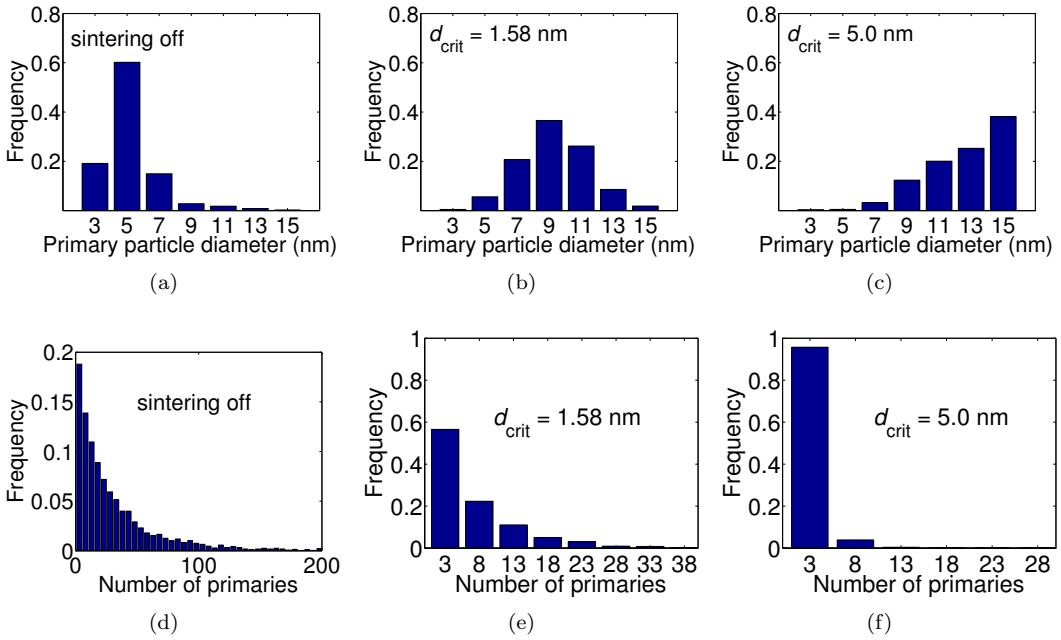

Figure 8: Effect of d_{crit} on primary particle size distribution ((a), (b), (c)) and distribution of the number of primaries per aggregate ((d), (e), (f)) for $H_{\mathrm{p}} = 1.2$ cm.

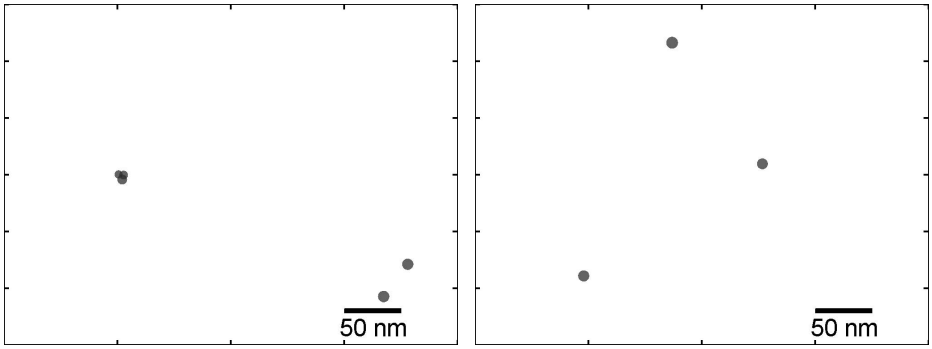

(a) $d_m = 10\,\mathrm{nm}, d_{\mathrm{crit}} = 1.58\,\mathrm{nm}$ (b) $d_m = 10\,\mathrm{nm}, d_{\mathrm{crit}} = 5.0\,\mathrm{nm}$

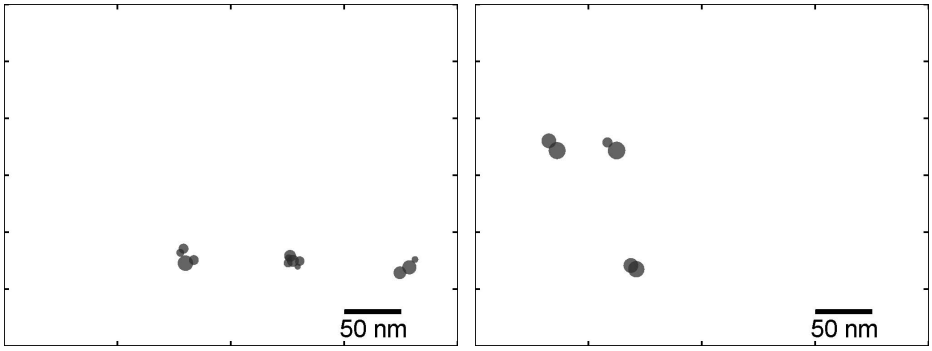

(c) $d_m = 20\,\mathrm{nm}, d_{\mathrm{crit}} = 1.58\,\mathrm{nm}$ (d) $d_m = 20\,\mathrm{nm}, d_{\mathrm{crit}} = 5.0\,\mathrm{nm}$

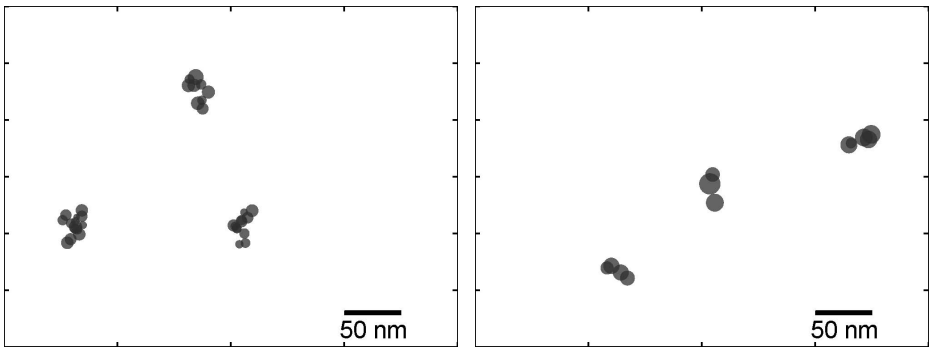

(e) $d_m = 30\,\mathrm{nm}, d_{\mathrm{crit}} = 1.58\,\mathrm{nm}$ (f) $d_m = 30\,\mathrm{nm}, d_{\mathrm{crit}} = 5.0\,\mathrm{nm}$

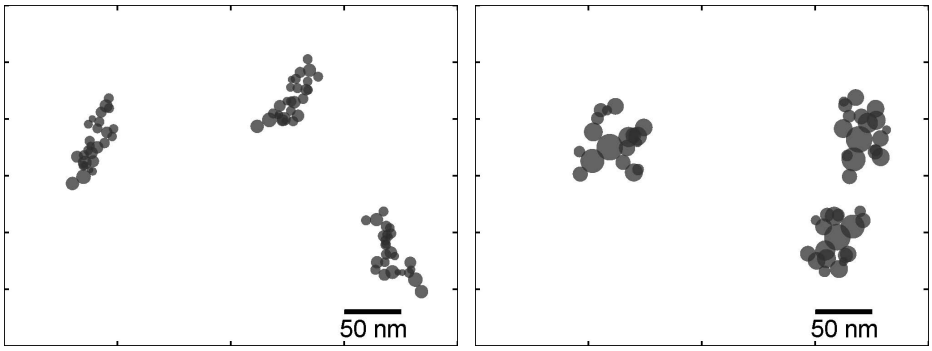

(g) $d_m = 50\,\mathrm{nm}, d_{\mathrm{crit}} = 1.58\,\mathrm{nm}$ (h) $d_m = 50\,\mathrm{nm}, d_{\mathrm{crit}} = 5.0\,\mathrm{nm}$

Figure 9: Simulated TEM images of particles with mobility diameter $d_m \approx 10$, 20, 30, 50 nm for $H_{\mathrm{p}} = 1.2$ cm. First column: $d_{\mathrm{crit}} = 1.58$ nm is used in the sintering model. Second column: $d_{\mathrm{crit}} = 5.0$ nm is used in the sintering model.

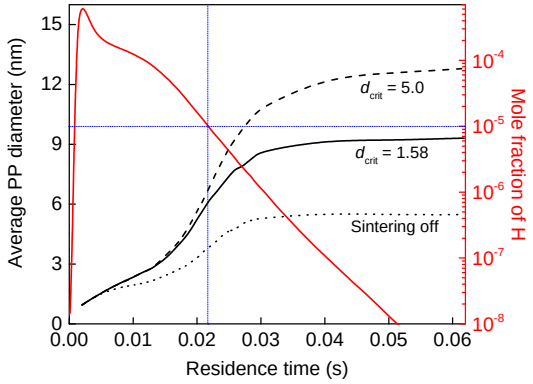

Figure 10: Average primary particle diameter (left Y-axis) and mole fraction of H atoms (right Y-axis) versus time (with different d_{crit} applied in the sintering model) for $H_{\mathrm{p}} = 1.2$ cm. The horizontal blue line shows an H mole fraction of 10^{-5}, while the vertical blue line indicates the corresponding residence time when the H mole fraction drops to 10^{-5}.

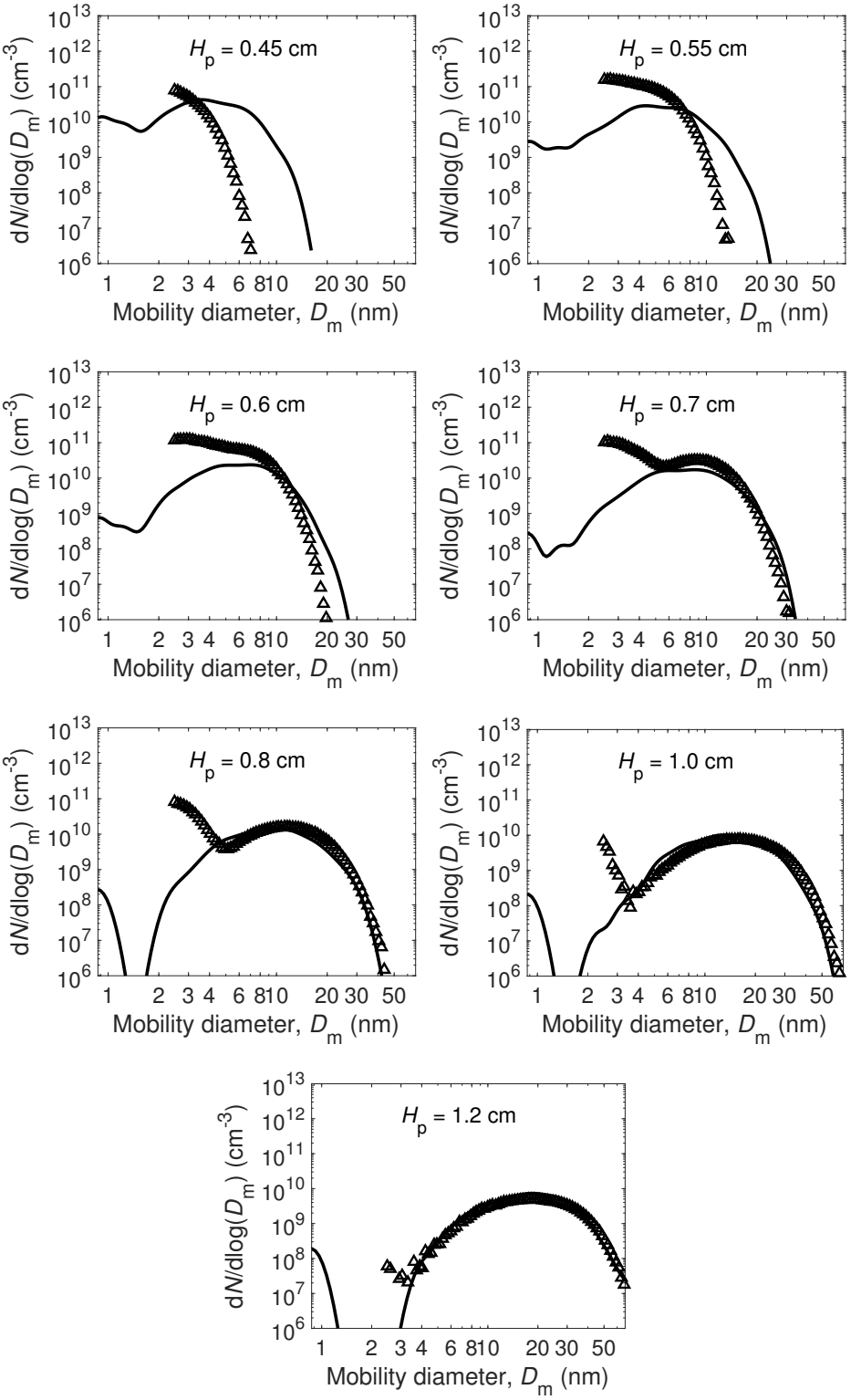

Figure 11: Computed PSDs (lines) at several H_p with the value of free model parameters listed in Table 1. Collision efficiency $A = 1$ in all simulations. Symbols are experimental data reported by Tsinghua in Ref. [7].

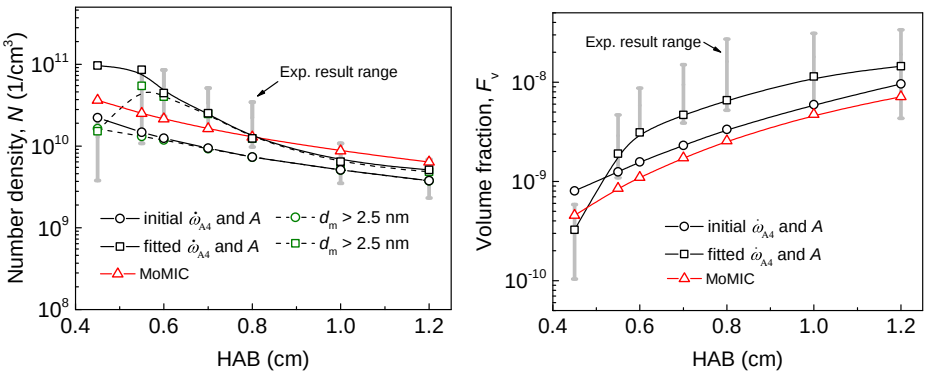

(a) (b)

Figure 12: Comparison between simulated (a) particle number density and (b) volume fraction and experimental results (shown by the error bars with the lower and upper limit being the minimum and maximum measured data among four individual experimental setup in Ref. [7]). Symbols (open circles, open squares and open triangles) are simulation results; lines are drawn to guide the eye. Green symbols are number density of particles with $d_m \geq 2.5$ nm.

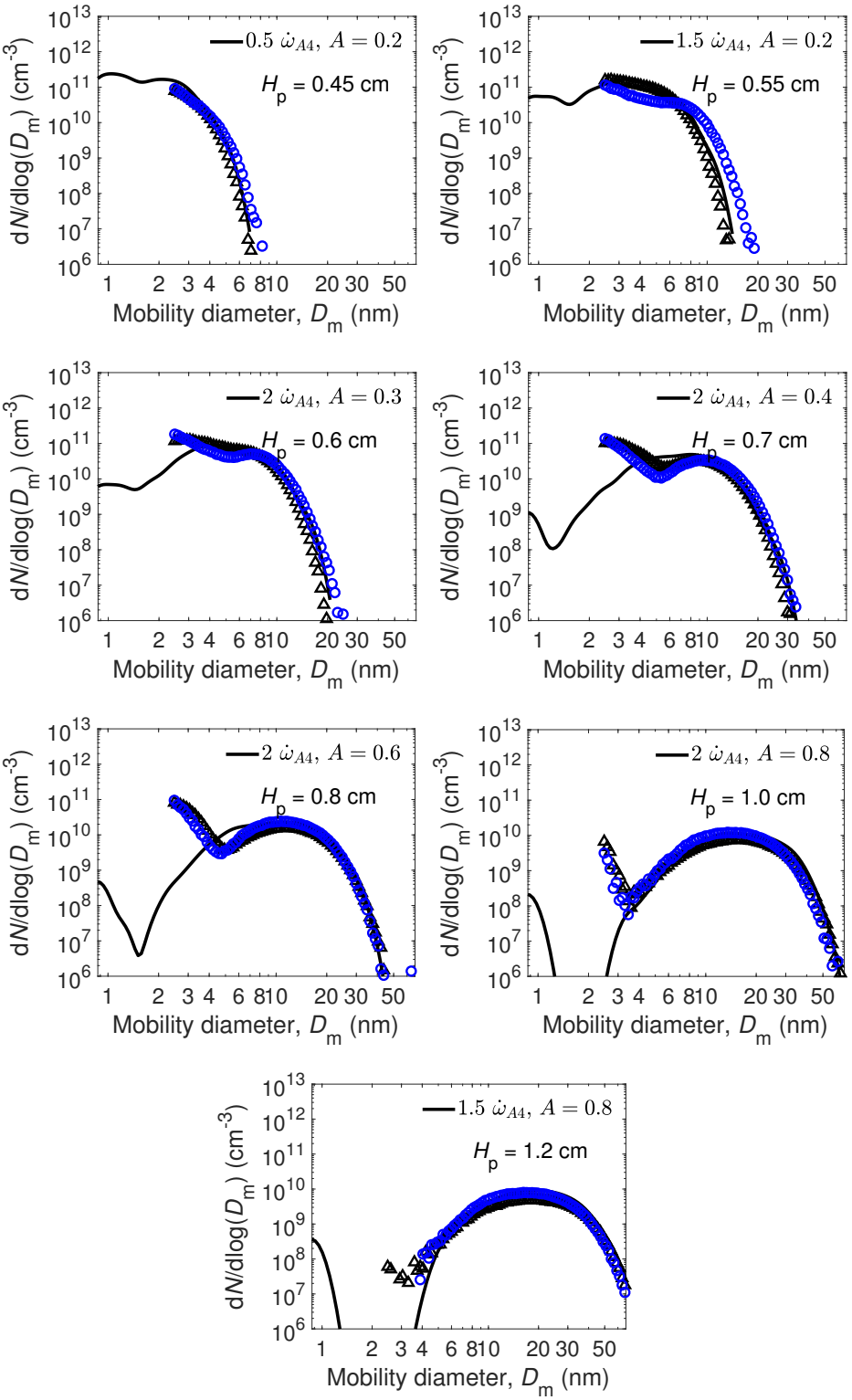

Figure 13: Computed PSDs (lines) with a constant multiplier applied to the rate of production of A4 ($\dot{\omega}_{A4}$) profile and collision efficiency (A) fitted for each individual H_p. Symbols are experimental data from Stanford 5.0 cm burner (blue open circle) and Tsinghua (black open triangle) in Ref. [7]

.